CFAR-Based Interference Mitigation for FMCW Automotive Radar Systems

Wang, Jianping

DOI
10.1109/TITS.2021.3111514

Publication date
2022

Document Version
Final published version

Published in
IEEE Transactions on Intelligent Transportation Systems

CFAR-Based Interference Mitigation for FMCW Automotive Radar Systems

Jianping Wang, *Member, IEEE*

***Abstract*— In this paper, constant false alarm rate (CFAR) detector-based approaches are proposed for interference mitigation of Frequency modulated continuous wave (FMCW) radars. The proposed methods exploit the fact that after dechirping and low-pass filtering operations the targets' beat signals of FMCW radars are composed of exponential sinusoidal components while interferences exhibit short chirp waves within a sweep. The spectra of interferences in the time-frequency (t-f) domain are detected by employing a 1-D CFAR detector along each frequency bin and then the detected map is dilated as a mask for interference suppression. The proposed approaches are applicable to the scenarios in the presence of multiple interferences. Compared to the existing methods, the proposed methods reduce the power loss of useful signals and are very computationally efficient. Their interference mitigation performances are demonstrated through both numerical simulations and experimental results.**

***Index Terms*— Beat signal, constant false alarm rate (CFAR) detector, FMCW radar, interference mitigation, time-frequency spectrum.**

I. Introduction

FREQUENCY modulated continuous wave (FMCW) radar has become a key device for automotive assistant/autonomous driving due to its operational capability in all day time and all weather conditions as well as its low cost. With the increase of vehicles equipped with radar sensors, the FMCW radar systems mounted on different cars in a busy area will inevitably suffer from strong interfering influence from the radar systems on the neighboring cars as well as other radars on the same car when they operate at the same time. The strong interferences would cause significantly increased noise floor, weak target mask, and reduced probability of target detection. Therefore, to overcome these risks, effectively mitigating interferences from other radars is critical to high-performance automotive radars.

Interference mitigation (IM) for automotive radar is a hot topic in recent years. In the literature, many approaches have been proposed and developed to suppress the interferences among different automotive radars, which can be classified into three categories: radar system coordination, radar system design and waveform design, and signal processing. For the radar system coordination approaches, a coordination scheme, which is either centralized [1] or distributed [2], [3], among different operational radars are devised to avoid conflicts by adjusting the operating parameters (i.e., transmitting time, spectrum, etc.) of each radar within the interfering area. Although these coordination schemes originated from communication networks could effectively avoid certain interferences, they usually require to introduce an extra coordination unit to the existing FMCW radar systems or need communication with a coordination center for a local distributed radar network.

On the other hand, some new radar system architectures and waveforms are proposed to benefit interference mitigation [4]–[10]. The frequency-hopping random chirp (FHRC) FMCW technique [4], [5] and FMCW radar with random repetition interval [6] resets the parameters of the chirp signals (the bandwidth, sweep duration, center frequency, repetition interval) every cycle to result in noise-like frequency responses of mutual interferences after the received signals are down-converted and demodulated. Both techniques would mitigate partial interferences and avoid the appearance of ghost targets caused by mutual interferences. However, the randomized repetition intervals would cause the Fast Fourier transform, which is conventionally used, inapplicable for the fast Doppler processing. On the other hand, pseudo-random noise signals [8] and chaotic sequences [7] are proposed to mitigate mutual interferences for automotive radars. For these radar systems, the received signals are processed by the correlation operation and a high sampling frequency is generally required for the Analog-to-Digital Converter (ADC), which would increase the cost of the radar systems. To exploit the advantages of both noise-like signals and the FMCW radar system, phase modulated (PM) FMCW radar systems modulate the FMCW waveforms with orthogonal or random sequences as transmitted signals [9], [10]. In reception, the received PM-FMCW signals can be down-converted as the traditional FMCW radars and then decoded by correlation with the stored sequences used for transmission modulation. The scattered signals resulting from the transmitted signals generally result in high correlation peaks while the uncorrelated interferences would spread out and build up the noise floor after decoding. The raised noise floor could overwhelm the weak targets and reduce the probability of detection. In addition, PM-FMCW radar cannot be easily implemented with existing FMCW radar chips and requires a new radar architecture to be designed.

Moreover, for the FMCW radars, a number of IM approaches have been developed, which include both

Manuscript received 24 February 2021; revised 8 July 2021; accepted 27 August 2021. Date of publication 20 September 2021; date of current version 9 August 2022. The Associate Editor for this article was C. F. Mecklenbräuker.

The author is with the Faculty of Electrical Engineering, Mathematics and Computer Science (EEMCS), Delft University of Technology, 2628 CD Delft, the Netherlands (e-mail: j.wang-4@tudelft.nl).

This article has supplementary downloadable material available at https://doi.org/10.1109/TITS.2021.3111514, provided by the authors.

Digital Object Identifier 10.1109/TITS.2021.3111514

traditional signal processing methods and deep learning-based methods. The traditional signal processing methods usually address the interference mitigation by filtering or separating the interferences from the received signals in various domains (i.e., space, time, frequency, time-frequency, etc). For an array-based radar system, interference mitigation can be achieved by constructing nulls in the directions of arrival (DOA) of the interferences through beamforming [11]–[13]. However, these approaches would suppress targets' signals scattered from the same DOAs of the interferences. In [14], the interference is detected based on a threshold and then suppressed by windowing in time. In [15], an iterative modified method based on empirical mode decomposition is proposed to decompose the low-pass filter output of an FMCW radar as a series of empirical modes in the time domain while in [16] the wavelet denoising method is used to separate interferences from the useful signals. Both approaches implicitly assume interferences are sparse in time in the received signals and their performances would degrade with the increase of the proportion of interference-contaminated samples in the acquired signal. By contrast, the Adaptive Noise Canceller (ANC) [17] is utilized to suppress interferences in the frequency domain. Although it is computationally very efficient, its performance heavily depends on if a proper correlated reference input of the adaptive filter can be found. Meanwhile, in [18] the interference-contaminated signal samples of FMCW radars are first to cut out in the short-time-Fourier-transform (STFT) domain and then a Burg-based method is developed to reconstruct the signal in the cut-out region based on an auto-regressive (AR) model along each frequency bin. However, with the increase of the cut-out region in the signal, the accuracy of the recovered signals with this approach drops rapidly. Moreover, recently some deep-learning approaches are used for interference mitigation of FMCW radars [19], [20]. These approaches generally require a large dataset acquired in various situations for training.

In this paper, we proposed a constant false alarm rate detector (CFAR)-based framework to mitigate interferences for FMCW radars. In this framework, the acquired beat signal is transformed into the time-frequency (t-f) domain by using the STFT. Then a one-dimensional (1-D) CFAR detector [21] is utilized to detect interferences and the detection map is dilated to generate a mask for interference suppression. In particular, one simplest approach is to use the generated mask to zero out the interference-contaminated samples. Another method is to keep their phases unchanged but correct their amplitudes by the mean of the amplitudes of the interference-free samples in the corresponding frequency bin based on the obtained mask. They are termed as the CFAR-Zeroing (CFAR-Z) and CFAR-Amplitude Correction (CFAR-AC) approaches, respectively. In addition, the Burg-based signal extrapolation [18] can be readily integrated in this framework for more accuracy signal reconstruction in each frequency bin, and the resultant approach is dubbed as CFAR-Burg for convenience. Compared to the existing approaches, the proposed approaches are capable to mitigate multiple interferences and minimize the power loss of useful signals. Their IM performance has been validated through both numerical simulations and experimental results. Moreover, they are very efficient and can be implemented for real-time IM of FMCW automotive radars.

The rest of the paper is organized as follows. Section II briefly describes the signal model of the FMCW radar. Then, the CFAR-based interference mitigation approaches are presented in section III.To demonstrate the interference mitigation performance of the proposed approach, numerical simulations and experimental results are shown in sections IV and V. Finally, some conclusions are drawn in section VI.

II. Signal Model and CFAR-Based Interference Mitigation Method

Assume that the transmitted signal $p(t)$ by an FMCW radar is given by

$$p(t) = e^{j2\pi\left(f_0 t + Kt^2/2\right)}, \quad 0 < t < T \tag{1}$$

where f_0, K and T represent, respectively, the starting frequency, sweep slope, and time duration of the FMCW signal. Considering the single bounce scattering, then the signals scattered back from point-like targets are the superposition of the time-delayed transmitted signals. Meanwhile, assume that the scattered signals from targets are contaminated by an interference $s_{\text{int}}(t)$ during its reception. After dechirping and low-pass filtering operating on receiver, the acquired beat signals is represented as

$$\begin{aligned} s(t) &= s_b(t) + \tilde{s}_{\text{int}}(t) + n(t) \\ &= \sum_{i=1}^{M} a_i e^{-j2\pi f_{b,i} t} + [s_{\text{int}}(t) \cdot \bar{p}(t)] * h_{lp}(t) + n(t) \end{aligned} \tag{2}$$

where $*$ denotes the convolution operation. $\bar{p}(t)$ denotes the complex conjugate of $p(t)$ and is used for dechirping. $h_{lp}(t)$ is the low-pass filter whose cut-off frequency is determined by the desired maximum detectable range of targets. $s_b(t) = \sum_{i=1}^{M} a_i e^{-j2\pi f_{b,i} t}$ is the beat signals of M scatterer, which is composed of M complex exponentials with the beat frequency $f_{b,i}$ and scattering coefficient a_i for the i^{th} scatterer. Note here, for conciseness, a_i subsumes a phase term $e^{j2\pi(K\tau_i^2/2 - f_0\tau_i)}$ resulting from the dechirping operation as well as a possible weighting factor of the low-pass filter, where τ_i is the time delay of the scattered signal of the i^{th} scatterer. $\tilde{s}_{\text{int}}(t) = [s_{\text{int}}(t) \cdot \bar{p}(t)] * h_{lp}(t)$ is the remaining interference after dechirping and low-pass filtering, and $n(t)$ denotes system noise and measurement errors.

Based on the Fourier theory, one can generally express the interference $s_{\text{int}(t)} = \sum_l b_l e^{j2\pi f_l t}$. For each exponential component $b_l e^{j2\pi f_l t}$, after dechirping and low-pass filtering the output $[b_l e^{j2\pi f_l t} e^{-j2\pi(f_0\ t + Kt^2/2)}] * h_l\, p(t)$ is either zero or a chirp pulse. So, for any interference with the narrow-band, wideband, as well as FMCW waveform with a different sweep slope from that of the victim FMCW signal, its remaining part $\tilde{s}_{\text{int}}(t)$ exhibits as a superposition of some chirp-like pulses in the time domain after dechirping and low-pass filtering (see Fig. 1(a)) [22]. Therefore, after taking the STFT of $s(t)$, the t-f domain counterparts of the beat signals of scatterers show as straight lines along the corresponding frequency bins while interferences display as oblique lines, as illustrated

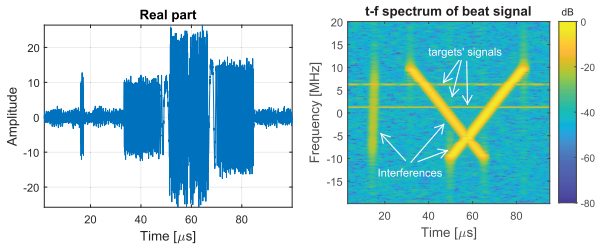

(a) (b)

Fig. 1. Illustration of (a) an interference-contaminated beat signal of an FMCW radar and (b) its spectrogram in the t-f domain.

in Fig. 1(b). These different distributions of useful beat signals and interferences motive us to proposed the CFAR-based IM approaches below. Note FMCW interferences with the same sweep slope and frequencies falling into the receiving bandwidth would result in ghost targets, but its probability of occurrence is extremely small [23]. This is a tricky case to IM for FMCW radars and dedicated approaches have to be developed, which is out of scope of this paper.

III. CFAR-Based Interference Mitigation Approaches

Accurately detecting interferences is crucial for effective interference mitigation. Based on the above analysis of different distribution features of useful signals and interferences in the t-f domain, i.e., straight lines for useful signals along the frequency bin and oblique lines for interferences, detecting interferences can be converted to distinguish the signals distributed along oblique lines relative to the frequency axis. Therefore, we propose to utilize a 1-D CFAR detector along each frequency bin in the t-f domain to detect interferences and then suppress them.

The complete CFAR-based IM approach is shown in Algorithm 1. In principle, it contains three main steps in implementation, which are described below in detail.

Algorithm 1 CFAR-Based Interference Mitigation Method

Data: Complex signal $\mathbf{s}$ in a sweep
Result: Complex signal $\mathbf{s}_c$ after interference mitigation
begin
  $\mathbf{S}_{tf} = \mathbf{STFT}(\mathbf{s})$; $[N_r, N_c] = \mathbf{size}(\mathbf{S}_{tf})$;
  $\mathbf{P}_{tf} = \mathbf{S}_{tf} \odot \mathbf{S}_{tf}^{*}$;
  for $k = 1$ **to** N_r **do**
    $\mathbf{D}(k, :) = \mathbf{CFARDetector}[\mathbf{P}_{tf}(k, :)]$;
  end
  $\mathbf{D}_{dl} = \mathbf{maskDilate}(\mathbf{D})$;
  /* Implement CFAR-Z, CFAR-AC or CFAR-Burg */
  // use the two lines below for CFAR-Z
  $\mathbf{S}_{tf}(\mathbf{D}_{dl}) = 0$; // Zeroing
  $\tilde{\mathbf{S}}_{tf} = \mathbf{S}_{tf}$;
  // use the line below for CFAR-AC
  $\tilde{\mathbf{S}}_{tf} = \mathbf{AmpCorrection}(\mathbf{S}_{tf}, \mathbf{D}_{dl})$
  // use the two lines below for CFAR-Burg
  $\mathbf{S}_{tf}(\mathbf{D}_{dl}) = 0$;
  $\tilde{\mathbf{S}}_{tf} = \mathbf{BurgExtrapolation}(\mathbf{S}_{tf}, \mathbf{D}_{dl})$;
  // to convert back to the time domain
  $\mathbf{s}_c = \mathbf{ISTFT}(\tilde{\mathbf{S}}_{tf})$;
end

A. Time-Frequency Analysis With the STFT

Applying the STFT to the acquired signal in (2), its t-f spectrum is obtained as

$$S(\tau, f) = \int_{-\infty}^{\infty} s(t) w(t-\tau) e^{-j2\pi f t} dt \tag{3}$$

where $w(\tau)$ is the window function, for instance, a Gaussian window or Hann window. For N discrete signal samples $s[k] = s(k\Delta t)$, $k = 0, 1, \ldots, N-1$, the discrete t-f spectrum samples over a regular grid are generally computed by

$$\begin{aligned} S_{tf}[m, n] &= S(m\Delta\tau, n\Delta f) \\ &= \sum_{k=0}^{N-1} s(k\Delta t) w(k\Delta t - m\Delta\tau) e^{-j2\pi nk\Delta f \Delta t} \Delta t \end{aligned} \tag{4}$$

where Δt is the time sampling interval, $\Delta\tau$ is the sliding step of the window and Δf is the step of frequency samples. One can see that for a fixed time delay $m\Delta\tau$ of the window, (4) can be efficiently implemented by using the fast Fourier transform (FFT). For the convenience of computation, generally $\Delta\tau = l \cdot \Delta t$ and $l \geq 1$ is an integer. Sliding the window over the signal duration, the t-f spectrum is obtained as a two-dimensional matrix with dimensions of $N_t \times N_f$ along the time and frequency axes, respectively, where N_t is the number of sliding steps of the time window and N_f is the number of FFT points.

Then, the spectrogram is obtained as the amplitude squared of the t-f spectrum, given by

$$P_{tf}[m, n] = \left| S_{tf}[m, n] \right|^2 = S_{tf}[m, n] \cdot \bar{S}_{tf}[m, n] \tag{5}$$

where $\bar{S}_{tf}$ is the complex conjugate of S_{tf}.

B. CFAR Detection and Detection Mask Dilation

In this step, the aim is to detect interferences. As the spectra of interferences are generally much stronger than those of useful signals (otherwise, interference mitigation becomes not very necessary), the Cell Averaging CFAR (CA-CFAR) detector [21] can be used to detect the peaks of signal spectra in each frequency bin in the t-f domain. By applying a CA-CFAR detector to the spectrum density along each frequency bin, a detection map $\mathbf{D}$ can be obtained, which is a matrix with the same size as the spectrogram. The detection matrix $\mathbf{D}$ has the entries of ones and zeros, and the ones indicate the positions of the detected spectral peaks in each frequency bin, i.e., the spectra of the detected interferences. The numbers of guard cells and training cells, the probability of false alarm, and the threshold factor of the CFAR detector can be set based on the different scenarios.

After acquiring the detection map with the CFAR detector, in principle, it could be employed as a mask to

suppress interferences. However, due to the possible existence of several interference-contaminated spectral samples in a frequency bin, a relatively large threshold value would be calculated; thus, it causes the missed detection of some edge cells of the interferences. To overcome this problem, a dilation procedure [24], which is widely used for image processing, is exploited to slightly swell the detected mask of interferences. By using a disk-shaped/octagonal structuring element, a pattern I formed by the one-valued pixels (i.e., the detected interference-contaminated samples) in the detection map $\mathbf{D}$ is dilated to be I_{dl} and the dilated detection map $\mathbf{D}_{dl}$ is obtained.

C. Interference Mitigation and Signal Recovery

The dilated detection map of interferences $\mathbf{D}_{dl}$ can be used as a mask for interference mitigation. With the aid of the dilated detection map, a simple interference mitigation approach is to zero out the interference-contaminated signal samples in the t-f spectrum S_{tf}, named as CFAR-Z for conciseness. However, the zeroing operation suppresses not only interferences but also the useful signals, thus causing the power loss of the targets' signals.

To circumvent the signal power loss of the CFAR-Z method, we suggest utilizing the amplitude correction method [25] to the interference-contaminated samples based on the CFAR detection map. The resultant approach is termed as CFAR-AC. The basic idea of this approach is to replace the amplitudes of the interference-contaminated samples with the average amplitude of the interference-free spectrum samples in the corresponding frequency bin but keep their phases invariant. The recovered value for an interference-contaminated sample $S_{tf}[m_i, n_i]$ is given by

$$\tilde{S}_{tf}[m_i, n_i] = A_{n_i} e^{j \arg(S_{tf}[m_i, n_i])} \tag{6}$$

$$A_{n_i} = \frac{1}{N_{\mathcal{L}_{n_i}}} \sum_{l \in \mathcal{L}_{n_i}} \left| S_{tf}[l, n_i] \right| \tag{7}$$

$$\mathcal{L}_{n_i} = \{ l | l = 1, 2, \ldots, N_t \ \& \ \mathbf{D}[l, n_i] = 0 \} \tag{8}$$

where $\tilde{S}_{tf}[m_i, n_i]$ is the recovered value of the sample at the position $[m_i, n_i]$ obtained after interference mitigation, and $\arg(x)$ takes the phase of a complex number x. $\mathcal{L}_{n_i}$ denotes the set of indices of the interference-free samples in the ${n_i}^{\text{th}}$ frequency bin and has $N_{\mathcal{L}_{n_i}}$ elements. So, the recovered amplitude A_{n_i} significantly suppresses strong interferences in the ${n_i}^{\text{th}}$ frequency bin. Repeating the same processing for all the frequency bins, the amplitudes of all the interference-contaminated samples can be corrected and the interferences are dramatically suppressed. Note the phases of these samples could be still disturbed by the interferences.

On the other hand, after taking the CFAR-Z operation on the spectrum in the t-f domain, the Burg-based extrapolation method [18] as well as other extrapolation approaches [22] can be readily exploited to reconstruct the eliminated samples of useful signals, which could overcome the possible phase disturbances in CFAR-AC and potentially get more accurate reconstruction of the removed samples of useful signals. This integrated approach of the CFAR detection and the Burg-based extrapolation is dubbed as the CFAR-Burg. For conciseness, the Burg-based extrapolation is omitted here and more details can be referred to [18].

After suppressing and/or reconstructing the interference-contaminated samples, an inverse STFT (ISTFT) is applied to the interference-mitigated t-f spectrum to reconstruct the targets' beat signals in the time domain.

In addition, we should mention that although the phases of the recovered samples still suffer from the disturbance of interferences, their effects are negligible after taking further coherent range compression and/or Doppler processing. Moreover, for the array signals contaminated simultaneously by the same interferences, the CFAR-AC approach has no impact on the beamforming performance as the phases of signals are kept unchanged.

TABLE I
PARAMETERS FOR NUMERICAL SIMULATIONS

Parameter	Victim radar	Aggressor radars
Center frequency [GHz]	77	77, 77, 77
Bandwidth [MHz]	600	660, 1200, 540
Sweep slope [MHz/μs]	6	6.6, -12, 5.4
Sweep duration [μs]	100	100, 100, 100
Maximum detection range [m]	250	N/A
Sampling frequency [MHz]	40	N/A

IV. NUMERICAL SIMULATIONS

Numerical simulations are presented to demonstrate the interference mitigation performance of the proposed approaches. Meanwhile, the results are compared with two state-of-the-art approaches, i.e., the Wavelet Denoising (WD) approach [16] and the Adaptive Noise Canceller (ANC) approach [17].

A. Performance Metrics

To facilitate the comparison among different IM approaches and quantitatively evaluate the accuracy of the beat signals recovered by each approach, we use as the metrics the Signal to Interference plus Noise Ratio (SINR) and correlation coefficient (ρ) [22] of the beat signal obtained after IM processing relative to the clean reference signal. The SINR and ρ are defined as [22]

$$\text{SINR}(\mathbf{s}_b, \hat{\mathbf{s}}) = 20 \log_{10} \frac{\|\mathbf{s}_b\|_2}{\|\hat{\mathbf{s}} - \mathbf{s}_b\|_2} \tag{9}$$

$$\rho(\mathbf{s}_b, \hat{\mathbf{s}}) = \frac{\hat{\mathbf{s}}^H \mathbf{s}_b}{\|\mathbf{s}_b\|_2 \cdot \|\hat{\mathbf{s}}\|_2} \tag{10}$$

where $\mathbf{s}_b$ and $\hat{\mathbf{s}}$ are respectively the vectors of the reference signal and the reconstructed beat signal after IM. Note the SINR defined in (9) is inversely proportional to the error vector magnitude in [26].

B. Point Target Simulation

Some typical automotive radar parameters were used for numerical simulations, as listed in Table I. Four point targets were placed in the scene of illumination at the distances

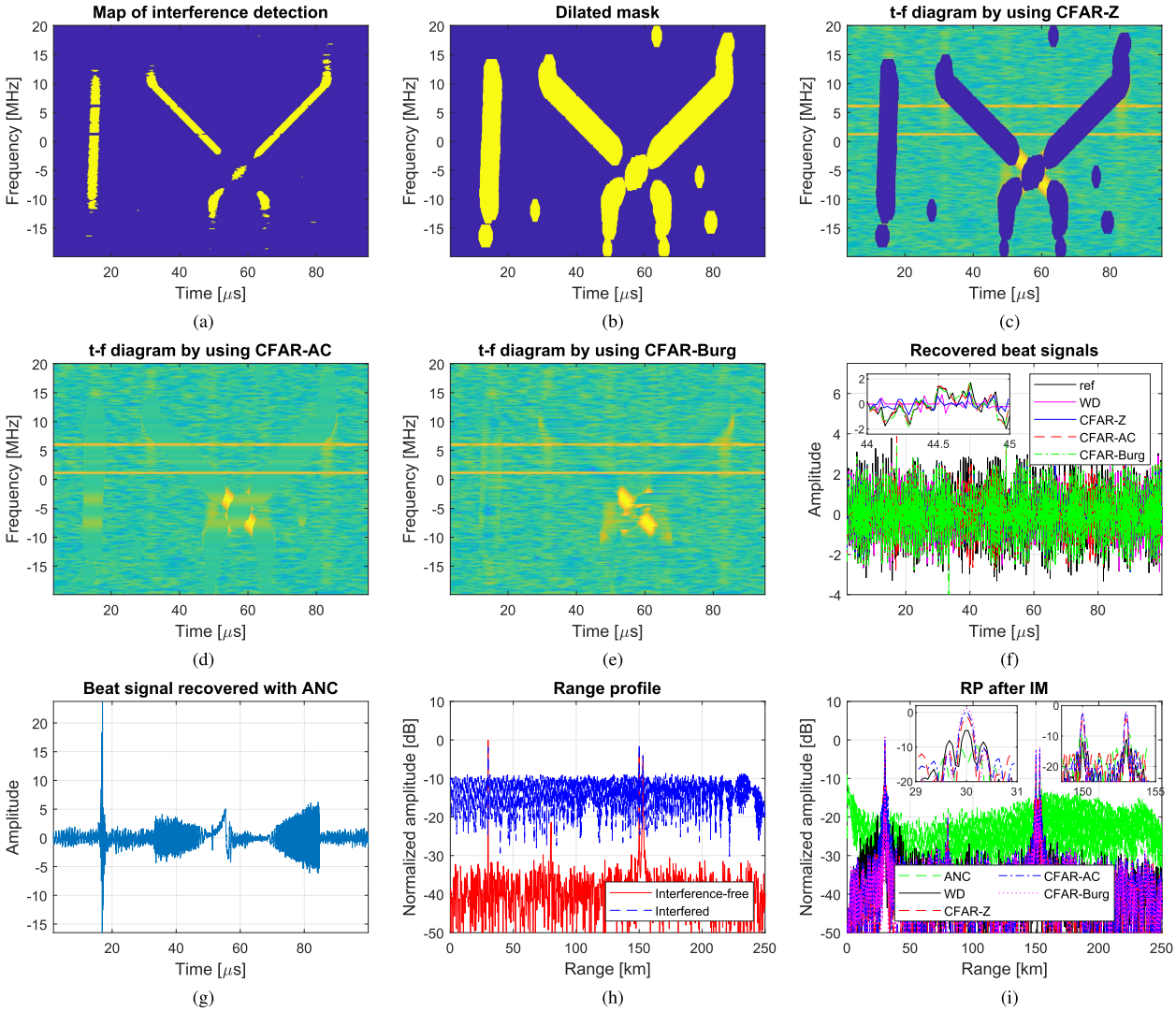

Fig. 2. Illustration of the CFAR-based interference mitigation and comparisons with the ANC and WD methods. (a) displays the map of the detected interferences and (b) is its dilated version. (c)-(e) are the t-f domain spectra after interference mitigation with CFAR-Z, CFAR-AC, and CFAR-Burg approaches. (f) shows the recovered beat signals after IM with the WD, CFAR-Z, CFAR-AC and CFAR-Burg approaches while (g) illustrates the recovered beat signal obtained with the ANC method. (h) and (i) present the range profiles of targets constructed by using the acquired raw signal and the recovered signals after IM, respectively.

of 30 m, 80 m, 150 m and 153 m, respectively. The victim radar transmitted up-sweep FMCW signals, and the scattered signals from these four scatterers had the amplitudes of 1, 0.1, 0.7 and 0.7 with random phases generated from a uniform distribution $[0, 2\pi]$. The scattered signals were also contaminated by three strong FMCW interferences with amplitudes of 10, 10, and 15, respectively. Complex white Gaussian noise with the signal to noise ratio (SNR) of 5 dB was added to account for thermal noise and measurement errors of the radar system. Thus, it leads to a synthetic beat signal with the SINR of -17.48 dB, as shown in Fig. 1(a). Due to the strong interferences, the weak target at the distance of 80 m is completely overwhelmed by the increased noise floor of the range profile formed by taking the FFT of the acquired signal (see Fig. 2(h)).

Using the proposed approaches to mitigate the interferences, the acquired time-domain signal is first transformed into the t-f domain by using the STFT with a 256-point sliding Hamming window and hop steps of 4 samples. The obtained t-f spectrogram is shown in Fig. 1(b), where the strong spectrum along the oblique lines are the interferences while the weak horizontal lines at the frequency bins of 1.2 MHz, 3.2 MHz and 6 MHz represent the useful beat signals. However, due to the weak scattered signal from the target at the distance of 80 m, the associated horizontal line at the frequency bin of 3.2 MHz is almost invisible.

Then, a CA-CFAR detector with 50 guard cells and 150 training cells on both sides of the cell under test and the probability of false alarm of 10^{-6} was utilized along each frequency bin and the non-horizontal patterns of interferences are detected (see Fig. 2(a)). As the threshold of the CA-CFAR detector is computed based on the average of training cells and varies for each Cell Under Test (CUT), it causes the missed detection of the cells at the edges of the oblique lines of the

interferences (i.e., the detected lines are thinner than that of the interferences), which leads to only partial mitigation of interferences in the following operations. To overcome this problem, the detection map of the CFAR detector was dilated by using the octagonal structuring element with a distance of 12 (pixel) units from its center to the sizes, as shown in Fig. 2(b). It is clear that the dilated detection map is much thicker compared to that in Fig. 2(a).

Next, by using the dilated detection map as a mask, the interference-contaminated samples can be cut-out or recovered with the CFAR-Z, CFAR-AC and CFAR-Burg methods. For the CFAR-Burg, a model order of five was used for signal reconstruction in each frequency bin with the Burg-based method. The obtained t-f spectra after IM are shown in Fig. 2(c)-(e). Finally, applying the ISTFT to the obtained t-f spectra, the corresponding beat signals were recovered, as shown in Fig. 2(f). For comparison, the IM of the signal was also performed using the ANC [17] and the WD methods [16]. For the ANC method, the length of the adaptive filter was set to be 80. Meanwhile, for the WD approach, the level of the wavelet decomposition was four which was optimally selected and the Stein's unbiased risk estimate was used to determine the threshold value. The beat signals recovered by the WD method is shown in Fig. 2(f) while the counterpart obtained with the ANC is separately presented in Fig. 2(g) considering its large amplitude. From Fig. 2(f) and its inset, one can see that the CFAR-Z approach suppresses not only the interferences but also the targets' beat signals at the time instances around the intersection points of the t-f spectra of the interferences and useful signals. Similarly, the wavelet denoising method also causes power loss of useful signals (see the inset in Fig. 2(f)). By contrast, the CFAR-AC and CFAR-Burg recover the beat signals of targets with very good agreements with the reference signal. From Fig. 2(g), the ANC method only suppresses part of the interferences between 35 μs and 85 μs and some chirp-like pulses of the interferences are still observed. This could be caused by the fact that the assumption of the complex conjugate symmetry of the interference spectrum around the zero used by the ANC method is not valid to the synthetic data. To quantitatively compare the accuracy of the recovered beat signals relative to the reference, the SINRs of the signals obtained with the ANC, WD, CFAR-Z, CFAR-AC and CFAR-Burg methods are -5.96 dB, 0.81 dB, 4.43 dB, 5.37 dB and 6.60 dB, respectively. And the corresponding correlation coefficients are $0.0865e^{-j0.6394}$, $0.5037e^{j0.0280}$, $0.8066e^{j0.0148}$, $0.8629e^{j0.0563}$ and $0.8964e^{j0.0152}$.

Taking the FFT of the recovered beat signals, the targets' range profiles (RP) in Fig. 2(i) are obtained. All the approaches except the ANC method significantly suppress the interferences and reduce the noise floor of the focused range profile compared to that before IM [see the "interfered" RP in Fig. 2(h)]. As a result, the weak target at the distance of 80 m is clearly visible after IM. Meanwhile, in contrast to the WD method, the CFAR-Z, CFAR-AC and CFAR-Burg methods all result in lower noise floors and lower sidelobes in the formed RPs (see the inset in Fig. 2(i)). Moreover, the CFAR-AC and CFAR-Burg methods correct or reconstruct the samples in the interference-contaminated region and overcome the power losses of targets' signals compared to the CFAR-Z method. As the Burg-based extrapolation recovers both the amplitudes and phases of the signal samples in the interfered area, the CFAR-Burg method leads to a RP with lower sidelobes than that obtained with the CFAR-AC. Therefore, in terms of the noise floor, power loss, and sidelobe levels of the resultant range profile, the CFAR-Burg achieves the best interference mitigation performance among the three CFAR-based approaches.

C. Effect of SNR on Interference Mitigation

The noise included in the acquired signal impacts the detection of interferences, thus affecting interference mitigation. In this section, we used the same targets' signals and the interferences as in section IV-B but changed the added noise levels to investigate the effect of SNR on the IM performance of the CFAR-based approaches and their competing counterparts, i.e., the WD and ANC methods.

The noise levels with the SNR ranging from -25 dB to 10 dB were considered and 500 times Monte Carlo runs were performed at each noise level. The CFAR-based methods were implemented using the same parameters of STFT and CFAR detector as in section IV-B. The statistics of the performance metrics achieved by the five IM methods are presented as the box plot in Fig. 3. The bottom and top of each box indicate the 25^{th} and 75^{th} percentiles of the samples, respectively. Meanwhile, the lines extending above and below each box show the range between the maximum and minimum values of the samples. Fig. 3(a) shows that the SINR of the recovered signals after IM increases with the rise of SNR of the input signal. In the current setup, the proposed CFAR-based methods, i.e., CFAR-Z, CFAR-AC and CFAR-Burg, achieve better SINR than the WD and ANC approaches when SNR ≥ -20 dB. As the interferences are almost overwhelmed by the noise when SNR < -20 dB, a large portion of the interferences was not detected by the CFAR detector; thus, the interferences could not be fully suppressed. Meanwhile, the WD method fails to extract the interferences and leads to degraded SINRs after IM. By contrast, the ANC method eliminates half of the frequency spectrum that does not contain targets' signals and uses the complex conjugate symmetry of the interference spectra to suppress them; thus, it results in better SINR after IM when the SNR of the input signal is very low. In addition, compared to the CFAR-AC and CFAR-Burg, the CFAR-Z obtains slightly higher SINRs when SNR $<$ 0 dB but lower ones when SNR $>$ 0 dB. This is because that when SNR $<$ 0 dB the intensities of targets' signals at the interference-contaminated region are closer to zero than to the amplitude-corrected/recovered values in which noise is the dominant component. Therefore, in terms of the SINR obtained after IM, the CFAR-Z approach is a better option than the CFAR-AC and CFAR-Burg when the SNR of the input signal is lower than 0 dB.

Moreover, Fig. 3(b) shows that the magnitudes of correlation coefficients of the signals obtained with the CFAR-AC and CFAR-Burg are constantly larger than that acquired by the

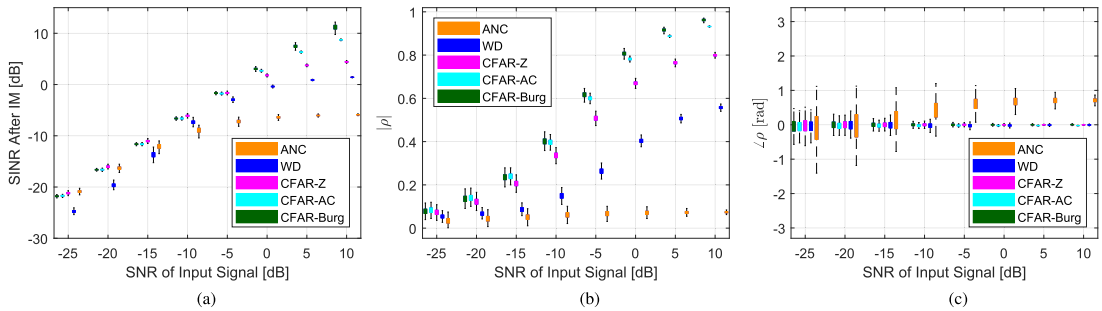

Fig. 3. Quantitative comparison of the interference mitigation performance of the ANC, WD, CFAR-Z, CFAR-AC, and CFAR-Burg methods at the different SNRs of the input signals. (a), (b) and (c) show the variations of SINRs, the magnitudes and phase angles of correlation coefficients of the recovered beat signals after interference mitigation, respectively.

TABLE II
COMPUTATIONAL TIME OF THE ANC, WD, CFAR-Z, CFAR-AC, AND CFAR-BURG APPROACHES FOR INTERFERENCE MITIGATION

	ANC	WD	CFAR-Z		CFAR-AC		CFAR-Burg	
			hp-4 [1]	hp-8	hp-4	hp-8	hp-4	hp-8
Time [ms]	72	10.8	154	79.6	165.7	87.3	613.8	386.3

*hp-4 and hp-8 represent hop steps of 4 and 8 of the 256-point sliding window for the STFT, respectively.

other three methods. Moreover, with the rise of the SNRs of input signals, the phase angles of the correlation coefficients of the recovered signals by the WD, CFAR-Z, CFAR-AC and CFAR-Burg all asymptotically approach zero. So in terms of both the SINRs and ρ's of the recovered signals after IM, the proposed CFAR-based approaches outperform the other two methods (i.e., the ANC and WD) and the CFAR-Burg achieves the best IM performance at a moderate SNR with the expense of higher computational load compared to the CFAR-AC.

D. Computational Time

The computational complexities of the proposed CFAR-Z and CFAR-AC are dominated by the CFAR detection along each frequency bin while the computational time of the CFAR-Burg is mainly consumed for data extrapolation with the Burg method.[1] In section IV-B, the synthetic beat signal in one sweep contains 3933 samples and was processed with the five approaches by using MATLAB 2019b on a computer with Intel i5-3470 CPU @ 3.2 GHz and 8 GB Random Access Memory (RAM). The computational time of the five IM approaches is summarized in Table II. One can see that the WD method is the most efficient one compared to the other four approaches. Meanwhile, when the hop step of the sliding window of the STFT increases from 4 to 8, the computational time of CFAR-based approaches decreases by about 50% as the number of samples in each frequency bin in the t-f domain is halved. So by properly adjusting the parameters of the STFT, the computational time of the CFAR-based approaches can be significantly reduced. Moreover, as the CFAR detection and signal reconstruction are carried out independently along each frequency bin in the t-f domain, these operations along different frequency bins can be implemented by parallel computing, which would further reduce their computational time and improve the real-time processing capability.

[1]In this paper, a constant model order, for simplicity, was used in all frequency bins for signal reconstruction with the Burg-based method. In practice, the model order in each frequency bin needs to be estimated, which would increase the computational time of the CFAR-Burg.

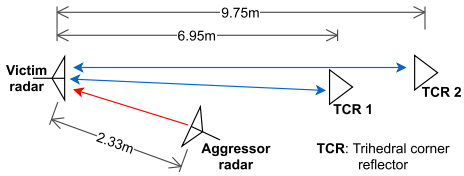

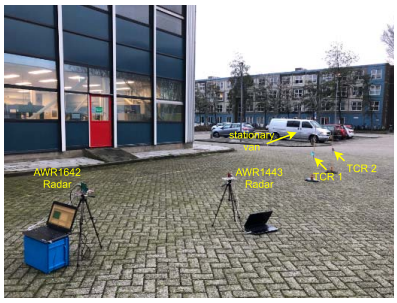

Fig. 4. Experimental setup for interference mitigation with two TI automotive radar boards. (a) shows geometrical configuration and (b) the experimental setup.

V. EXPERIMENTAL RESULTS

In this section, the experimental results are presented to demonstrate the performance of the proposed approach.

One Texas Instruments (TI) AWR1642BOOST radar board and a TI AWR1443BOOST radar module were used as a victim radar and an aggressor radar, respectively. Both radar modules include onboard-etched microstrip antennas for the transmitters and receivers. The field of view (FOV) of the victim radar in azimuth is from $-70°$ to $70°$. The aggressor radar was placed at a position of about $15°$ away from the broadside direction of the victim radar. Two Trihedral Corner Reflectors (TCRs) formed by three isosceles triangles with side edges of 8.5 cm are used as targets. The geometrical configuration and picture of experimental setup are shown in Fig. 4(a) and (b). The system parameters used for the

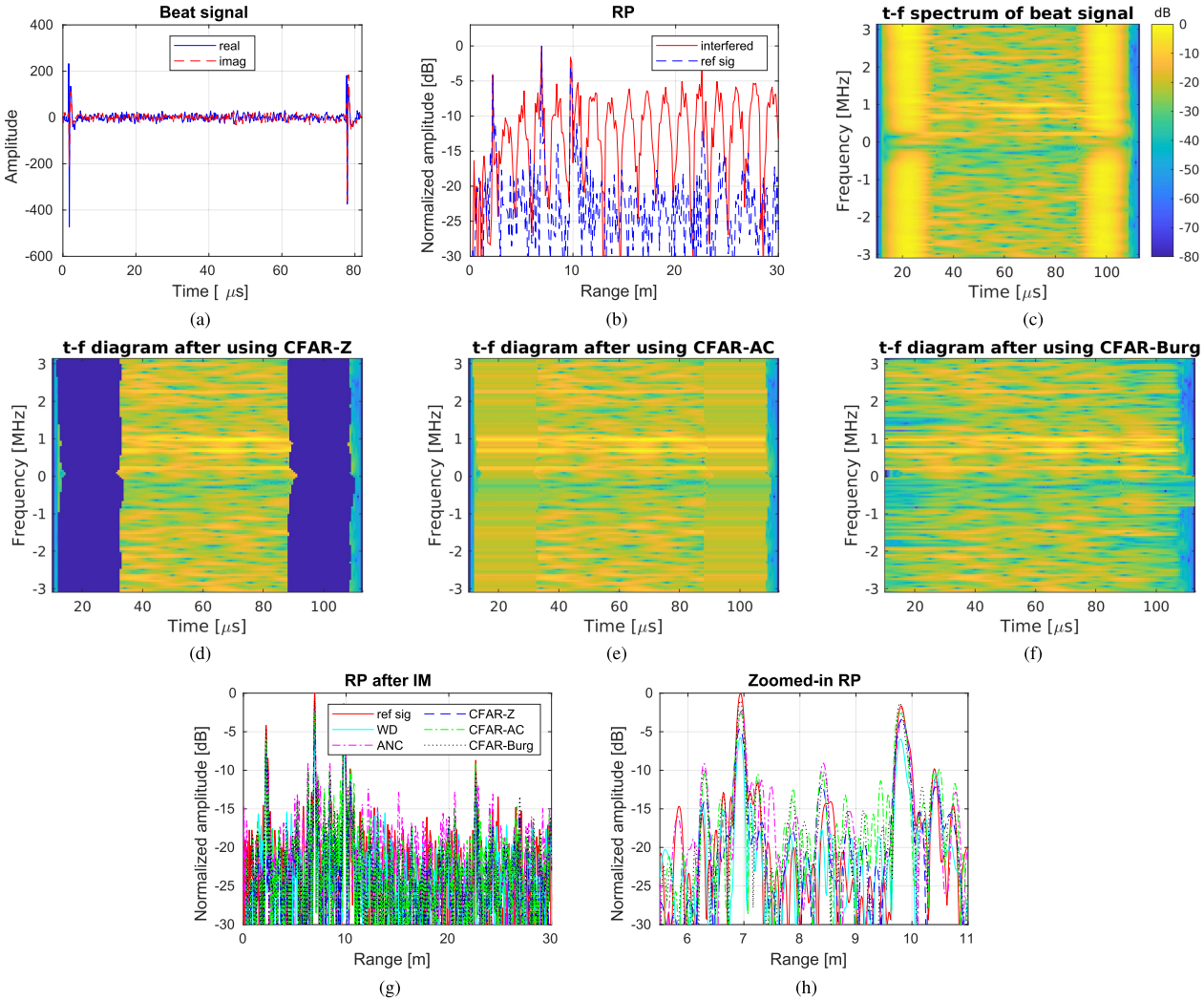

Fig. 5. Interference mitigation for the experimental radar measured with TI automotive radar. (a) shows the acquired beat signal contaminated by the interferences and (c) its time-frequency spectrum. (b) presents the range profiles of targets related to the beat signal in (a) and an interference-free reference. (d)-(f) give the results of IM with CFAR-Z, CFAR-AC and CFAR-Burg approaches, respectively. (g) displays the reference range profile and the ones obtained after IM and (h) shows the zoomed-in view of the range profiles at the distance of 5.5 m to 11 m.

TABLE III
PARAMETERS OF EXPERIMENTAL RADAR SYSTEMS

Parameter	Victim radar	Aggressor radar
Center frequency [GHz]	77.69	77.69
Bandwidth [MHz]	1380.18	1380
Sweep slope K [MHz/μs]	15.015	35
Sweep duration T [μs]	91.92	39.4337
Sampling frequency [MHz]	6.25	5
No. of Samples	512	256

victim and aggressor radars are listed in Table III. The AWR1642 radar board is connected with a TI DCA1000EVM data capture card to collect raw ADC data which is then sent to a host laptop for data storage.

Fig. 5(a) shows the acquired signal in one of the FMCW sweeps. Two large pulses are observed at the beginning and end of the acquired data, which are caused by the strong interferences from the aggressor radar. After range compression, the interference-contaminated signal leads to a range profile with significantly increased noise floor (see Fig. 5(b)). For comparison, the range profile of targets obtained with a reference signal is also presented, where the first three peaks indicate the locations of the aggressor radar and two TCRs at the distance of 2.33 m, 6.95 m and 9.75 m, respectively. One can observe that in the range profile obtained with the interference-contaminated signal the two TCRs are almost overwhelmed by the increased noise floor. This made the TCR at the further distance not detectable when a CA-CFAR detector was employed to the range profile for target detection (see Fig. 6(a)). The CA-CFAR detector was set with one guard cell and 10 training cells on each side of the CUT and the probability of false alarm of 1×10^{-4}.

To overcome the miss-detection of target caused by the strong interferences, the proposed approaches were applied to the acquired signal for interference mitigation. Firstly, the t-f spectrum of the acquired signal was computed through the

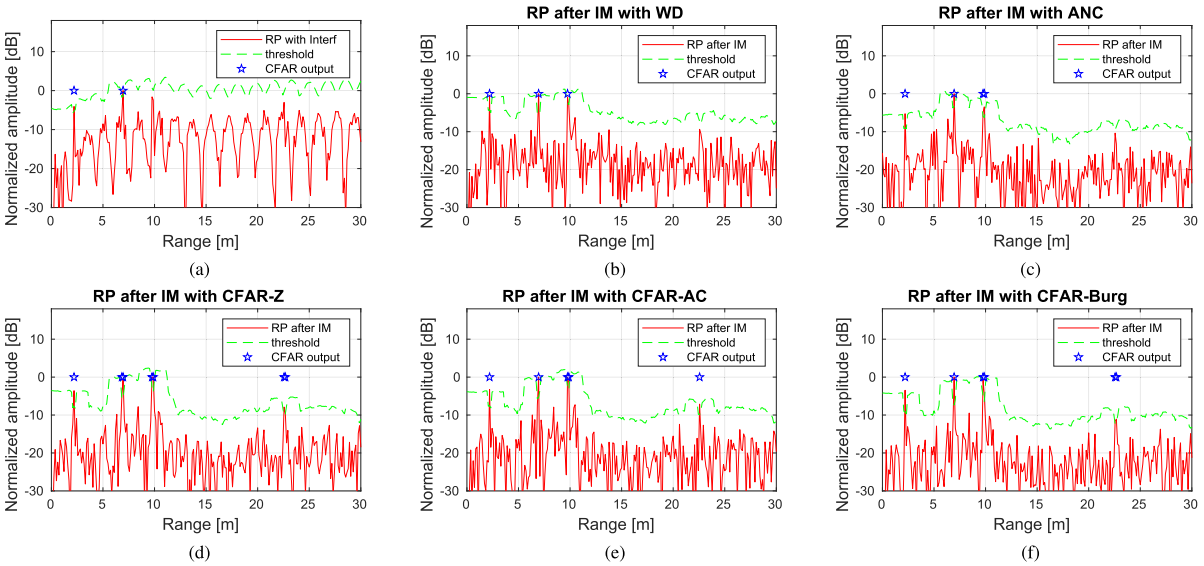

Fig. 6. The output results of the CFAR detection of the input range profiles before and after interference mitigation. (a) shows the detected results of the range profiles obtained with interference-contaminated signal. (b)-(f) are the corresponding detection results after taking interference mitigation with the WD, ANC, CFAR-Z, CFAR-AC and CFAR-Burg approaches, respectively.

STFT by using a 128-point sliding Hamming window with hop steps of four for signal segmentation and then taking the 128-point FFT of each segment. The obtained spectrum is shown in Fig. 5(c), where the interferences exhibit as the two thick vertical lines. Then, a 1-D CFAR detector with 50 training cells and 3 guard cells on each side of the CUT and the probability of false alarm of 1×10^{-4} was applied along each frequency bin to detect the interference-contaminated signal spectrum, and then the obtained detection map was dilated using the same octagonal structuring element as in section IV-B. After that, with the aid of the dilated detection map, the zeroing, amplitude correction and the Burg-based extrapolation with a model order of five were utilized to eliminate the inferences or recover the related signal samples, and the results of CFAR-Z, CFAR-AC and CFAR-Burg approaches are given in Fig. 5(d) and (e). Finally, the t-f domain spectra obtained after IM were inverted back to time domain through the ISTFT.

To demonstrate the IM performance of the proposed approaches, the targets' range profiles resulting from their recovered beat signals are shown in Fig. 5(g). For comparison, the range profiles obtained with the reference signal and the beat signals recovered by the WD and ANC are also presented, which are normalized by the maximum of all the range profiles. From Fig. 5(g), the range profiles obtained with the WD and three CFAR-based approaches have very good agreement with the reference while the one acquired by the ANC method has higher sidelobes. However, based on the zoomed-in view of the range profiles around the two TRCs (Fig. 5(h)), one can see that among the five IM methods, the CFAR-AC and CFAR-Burg methods get the peak values close to the reference ones at the distances of two TCRs. By contrast, the WD method results in the smallest peak amplitude as it not only eliminates the strong interferences but also removes part of the useful signal power. Among the CFAR-based methods, the CFAR-Z, as expected, leads to smaller peak values of the range profile at the positions of two TCRs due to the power loss of signals caused by the zeroing operation. So in terms of power conservation of useful signals, the CFAR-AC, CFAR-Burg and ANC methods achieve the best performance in this case. However, the ANC method assumes strict complex conjugate symmetry of the interference spectrum around the frequency of zero; otherwise, its performance degrades significantly as shown in section IV-B. In addition, it should be mentioned that to avoid the weighting effect of the sliding window of the STFT on the reconstructed signal samples at the two ends, 128 zeros were padded at both sides of the acquired signal before taking the STFT and the extra zeros were then removed after inverting the t-f spectrum through the ISTFT. Due to this operation before the STFT, it leads to the visually "increased" time duration of the t-f domain plots (i.e., Fig. 5(c)-(f)) compared to that of the acquired signal (Fig. 5(a)).

To further evaluate the quality of the beat signals recovered by the five IM approaches, the target detection performance of the constructed range profiles were tested by using the same CFAR detector as in Fig. 6(a). Fig. 6(b)-(f) show the output results of the CFAR detector. One can see that the three peaks related to the aggressor radar and two TCRs are all detected after IM with all the five methods while the TCR at the largest distance is missed based on the range profile before IM (Fig. 6(a)). So all the five IM methods improve the probability of detection of targets. Moreover, based on the range profiles obtained with the CFAR-based methods (i.e., CFAR-Z, CFAR-AC and CFAR-Burg), a fourth target, which is a stationary van at a distance of 22.5 m, is also detected (Fig. 6(d)-(f)) but missed when the RPs acquired with the WD and ANC methods were used (Fig. 6(b) and (c)). Therefore, the beat signals obtained with the proposed CFAR-based IM approaches provide higher target's probability

of detection than those recovered with the WD and ANC methods. Furthermore, the proposed CFAR-based IM approaches also work well in moving target scenarios and details can be seen in the supplementary material.

VI. Conclusion

In the paper, we proposed the CFAR-based approaches, i.e., CFAR-Z, CFAR-AC, and CFAR-Burg, to mitigate inference for FMCW radars system, which exploit the CFAR detector to detect the large chirp-pulse like interferences in the time-frequency domain and then apply the zeroing, amplitude correction and signal extrapolation approaches, respectively, to mitigate interferences. Compared to the prior art methods at which the interference in the beat-frequency signal is detected within a particular time interval, the CFAR-based approaches detect interferences in the 2-D "time-frequency" domain and achieve better interference mitigation performance in terms of both SINR and the correlation coefficient of the recovered signal after IM. Moreover, both CFAR-Z and CFAR-AC approaches are computationally efficient and could be implemented for real-time processing for automotive radars while CFAR-Burg could get more accurate reconstruction of signal samples contaminated by interferences at the expense of increased computational load. In addition, as the proposed CFAR-based approaches process the spectrum along each frequency bin separately, in principle they all could be accelerated through parallel computing.

Acknowledgment

The author would like to thank Y. Lu and I. R. Montero for their help with experimental data acquisition and acknowledge Prof A. Yarovoy for his feedback on the manuscript.

References

[1] J. Khoury, R. Ramanathan, D. McCloskey, R. Smith, and T. Campbell, "RadarMAC: Mitigating radar interference in self-driving cars," in *Proc. 13th Annu. Int. Conf. Sens., Commun., Netw.*, 2016, pp. 1–9.

[2] S. Ishikawa, M. Kurosawa, M. Umehira, X. Wang, S. Takeda, and H. Kuroda, "Packet-based FMCW radar using CSMA technique to avoid narrowband interefrence," in *Proc. Int. Radar Conf.*, Sep. 2019, pp. 1–5.

[3] C. Aydogdu, M. F. Keskin, N. Garcia, H. Wymeersch, and D. W. Bliss, "RadChat: Spectrum sharing for automotive radar interference mitigation," *IEEE Trans. Intell. Transp. Syst.*, vol. 22, no. 1, pp. 416–429, Jan. 2019.

[4] T.-N. Luo, C.-H. E. Wu, and Y.-J. E. Chen, "A 77-GHz CMOS automotive radar transceiver with anti-interference function," *IEEE Trans. Circuits Syst. I, Reg. Papers*, vol. 60, no. 12, pp. 3247–3255, Dec. 2013.

[5] X. Hu, Y. Li, M. Lu, Y. Wang, and X. Yang, "A multi-carrier-frequency random-transmission chirp sequence for TDM MIMO automotive radar," *IEEE Trans. Veh. Technol.*, vol. 68, no. 4, pp. 3672–3685, Apr. 2019.

[6] Y. Kitsukawa, M. Mitsumoto, H. Mizutani, N. Fukui, and C. Miyazaki, "An interference suppression method by transmission chirp waveform with random repetition interval in fast-chirp FMCW radar," in *Proc. 16th Eur. Radar Conf.*, 2019, pp. 165–168.

[7] E. Gambi, F. Chiaraluce, and S. Spinsante, "Chaos-based radars for automotive applications: Theoretical issues and numerical simulation," *IEEE Trans. Veh. Technol.*, vol. 57, no. 6, pp. 3858–3863, Nov. 2008.

[8] Z. Xu and Q. Shi, "Interference mitigation for automotive radar using orthogonal noise waveforms," *IEEE Geosci. Remote Sens. Lett.*, vol. 15, no. 1, pp. 137–141, Jan. 2018.

[9] F. Uysal, "Phase-coded FMCW automotive radar: System design and interference mitigation," *IEEE Trans. Veh. Technol.*, vol. 69, no. 1, pp. 270–281, Jan. 2020.

[10] E. H. Kim and K. H. Kim, "Random phase code for automotive MIMO radars using combined frequency shift keying-linear FMCW waveform," *IET Radar, Sonar Navigat.*, vol. 12, no. 10, pp. 1090–1095, Oct. 2018.

[11] J. Bechter, M. Rameez, and C. Waldschmidt, "Analytical and experimental investigations on mitigation of interference in a DBF MIMO radar," *IEEE Trans. Microw. Theory Techn.*, vol. 65, no. 5, pp. 1727–1734, May 2017.

[12] I. Artyukhin, V. Ermolaev, A. Flaksman, A. Rubtsov, and O. Shmonin, "Development of effective anti-interference primary signal processing for mmWave automotive radar," in *Proc. Int. Conf. Eng. Telecommun.*, Nov. 2019, pp. 1–5.

[13] M. Rameez, M. Dahl, and M. I. Pettersson, "Adaptive digital beamforming for interference suppression in automotive FMCW radars," in *Proc. IEEE Radar Conf.*, Apr. 2018, pp. 252–256.

[14] T. Nozawa *et al.*, "An anti-collision automotive FMCW radar using time-domain interference detection and suppression," in *Proc. Int. Conf. Radar Syst.*, 2017, pp. 1–5.

[15] J. Wu, S. Yang, W. Lu, and Z. Liu, "Iterative modified threshold method based on EMD for interference suppression in FMCW radars," *IET Radar, Sonar Navigat.*, vol. 14, no. 8, pp. 1219–1228, Aug. 2020.

[16] S. Lee, J.-Y. Lee, and S.-C. Kim, "Mutual interference suppression using wavelet denoising in automotive FMCW radar systems," *IEEE Trans. Intell. Transp. Syst.*, vol. 22, no. 2, pp. 887–897, Feb. 2019.

[17] F. Jin and S. Cao, "Automotive radar interference mitigation using adaptive noise canceller," *IEEE Trans. Veh. Technol.*, vol. 68, no. 4, pp. 3747–3754, Apr. 2019.

[18] S. Neemat, O. Krasnov, and A. Yarovoy, "An interference mitigation technique for FMCW radar using beat-frequencies interpolation in the STFT domain," *IEEE Trans. Microw. Theory Techn.*, vol. 67, no. 3, pp. 1207–1220, Mar. 2018.

[19] J. Mun, S. Ha, and J. Lee, "Automotive radar signal interference mitigation using RNN with self attention," in *Proc. IEEE Int. Conf. Acoust., Speech Signal Process.*, May 2020, pp. 3802–3806.

[20] J. Rock, M. Toth, P. Meissner, and F. Pernkopf, "Deep interference mitigation and denoising of real-world FMCW radar signals," in *Proc. IEEE Int. Radar Conf.*, Apr. 2020, pp. 624–629.

[21] M. A. Richards, *Fundamentals of Radar Signal Processing*, 2nd ed. New York, NY, USA: McGraw-Hill, 2014.

[22] J. Wang, M. Ding, and A. Yarovoy, "Matrix-pencil approach-based interference mitigation for FMCW radar systems," *IEEE Trans. Microw. Theory Techn.*, early access, Jul. 2, 2021, doi: 10.1109/TMTT.2021.3090798.

[23] G. Kim, J. Mun, and J. Lee, "A peer-to-peer interference analysis for automotive chirp sequence radars," *IEEE Trans. Veh. Technol.*, vol. 67, no. 9, pp. 8110–8117, Sep. 2018.

[24] R. C. Gonzalez, R. E. Woods, and S. L. Eddins, *Digital Image Processing Using MATLAB*. New York, NY, USA: Gatesmark, 2009.

[25] M. Wagner, F. Sulejmani, A. Melzer, P. Meissner, and M. Huemer, "Threshold-free interference cancellation method for automotive FMCW radar systems," in *Proc. IEEE Int. Symp. Circuits Syst.*, May 2018, pp. 1–4.

[26] M. Toth, P. Meissner, A. Melzer, and K. Witrisal, "Performance comparison of mutual automotive radar interference mitigation algorithms," in *Proc. IEEE Radar Conf.*, Apr. 2019, pp. 1–6.

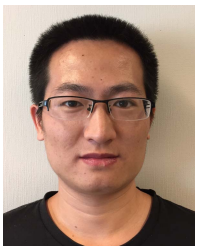

Jianping Wang (Member, IEEE) received the Ph.D. degree in electrical engineering from Delft University of Technology, the Netherlands, in 2018.

From August 2012 to April, 2013, he worked as a Research Associate with the University of New South Wales, Australia, on frequency modulated continuous wave synthetic aperture radar signal processing for formation flying satellites. He is currently a Post-Doctoral Researcher with the Group of Microwave Sensing, Signals and Systems (MS3), Delft University of Technology. His research interests include microwave imaging, signal processing, and antenna array design.

Dr. Wang was a TPC member of IET International Radar Conference, Nanjing, China, in 2018. He was a Finalist of the Best Student Paper Award in International Workshop on Advanced Ground Penetrating Radar (IWAGPR), Edinburgh, U.K., in 2017, and the International Conference on Radar, Brisbane, Australia, in 2018. He has served as a reviewer of many IEEE journals.